ACS APPLIED OPTICAL MATERIALS

pubs.acs.org/acsaom

Article

Investigation of Phase Transition and Ultrawide Band Gap Engineering in MgGaO Semiconductor Thin Films

Tianchen Yang, Chengyun Shou, Abdullah Almujtabi, Jason Tran, Qiyin Lin, Yuan Li, Quazi Sanjid Mahmud, Peng Wei, and Jianlin Liu*

Cite This: *ACS Appl. Opt. Mater.* 2023, 1, 1670−1678

Read Online

ACCESS | Metrics & More | Article Recommendations | Supporting Information

ABSTRACT: Magnesium gallium oxide (MgGaO) ternary alloys with band gap energy larger than ∼5.0 eV can provide opportunities for optoelectronics in the deep ultraviolet spectral range and power electronics with extremely high critical field strength. It is important to grow high-quality MgGaO alloys with varied Mg compositions and understand their structural and optical properties. From this perspective, 20 MgGaO samples with Mg atomic percentages from 0 to 100% were grown by using oxygen plasma-assisted molecular beam epitaxy. Band gap tuning from 5.03 to 5.89 eV was achieved for the ternary alloys, and all samples had a transmittance of over ∼90% in the visible spectral range. The lattice structures were confirmed to transform from the β phase in Ga-rich materials to the β and rocksalt mixture phase in high-Ga high-Mg alloys and to the pure rocksalt phase in Mg-rich alloys. How lattice parameters change with the increase of Mg atom % and the epitaxy relationship between MgGaO films and c-sapphire substrates were revealed.

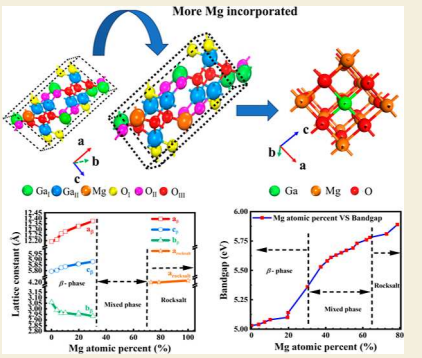

KEYWORDS: *magnesium gallium oxide, molecular beam epitaxy, phase transition, band gap engineering, ultrawide band gap semiconductor*

1. INTRODUCTION

Nowadays, wide band gap semiconductor materials such as gallium nitride (GaN) and silicon carbide (SiC) have been applied in many military and civilian fields, such as power electronics and deep ultraviolet (UV) optoelectronics.[1−5] To further enhance the performance in these areas, ultrawide band gap (UWBG) semiconductors with the band gap energies larger than those of GaN and SiC are desirable. As a promising candidate of UWBG semiconductors, β-Ga_2O_3 with a large direct band gap of ∼4.9 eV has been extensively studied due to its high physical and chemical stability, high critical electric field strength of ∼8 MV/cm, and high figure-of-merit.[6] Therefore, it has been widely used in power electronic and optoelectronic devices such as solar-blind UV photodetectors,[7−10] gas sensors,[11,12] and field effect transistors.[13−15] For broader and more extensive applications of β-Ga_2O_3, band gap engineering is highly desired. The tunable band gap paves the way for designing and optimizing electronic and optoelectronic devices with more flexibility and higher performance. Besides band gap tuning by modulating the crystalline disorder of Ga_2O_3 itself,[16] band gap-lowering candidates such as InGaO[17−21] with the band gap ranging from ∼3.88 to ∼5.0 eV and ZnGaO[22−24] with the band gap ranging from ∼4.7 to ∼5.1 eV have been widely used for solar-blind photodetectors[25,26] and thin-film transistors[27,28] already. On the other hand, as one of the band gap-increasing candidates, AlGaO[21,29−31] with the band gap ranging from 4.85 to 7.1 eV has been extensively studied as well. As an alternatively viable band gap-increasing candidate, β-MgGaO single-crystalline thin films with band gap tuning up to ∼5.22 eV were grown recently, and properties of their metal−semiconductor−metal photodetectors were investigated.[32] MgGaO can be construed as a mixture of Ga_2O_3 and MgO materials; thus, its band gap may be tuned between ∼4.9 and ∼7.8 eV.[32,33] However, the phase transition conditions to transform the crystal structure from the β phase to the mixed phase and finally to the rocksalt phase for the MgGaO alloy system with increasingly incorporated Mg are still not clear. The structural and optical properties of the films in different phases remain unknown. Thus, revealing the phase transition condition with band gap tuning of MgGaO thin films is of great significance for next-generation Ga_2O_3-based electronics and optoelectronics.

In this paper, 20 MgGaO thin-film samples with relative Mg/Ga atomic percent ranging from 0 at. %/100 at. % to 100 at. %/0 at. % were grown by plasma-assisted molecular beam epitaxy (MBE). Structure transformation, film quality, lattice parameters, surface morphology, optical band gap properties,

Received: July 9, 2023
Revised: September 5, 2023
Accepted: September 6, 2023
Published: September 20, 2023

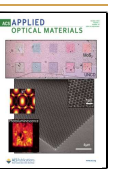

Table 1. Characterized Parameters of 20 MgGaO Thin Films with Mg Atom % from 0 to 100%

sample index	film thickness (nm)	relative atomic percent (EDX)		relative atomic percent (XPS)			phase identification	chemical formula	surface roughness (nm)	band gap (eV)
		Mg %	Ga %	Mg %	Ga %	O %				
#01	117.54	0	100	0	35.6	64.4	β-phase	Ga_2O_3	1.544	5.03
#02	122.17	3.86	96.14					$(Mg_xGa_{1-x})_2O_3$	2.058	5.04
#03	130.71	7.09	92.91	1.5	27.8	70.7			0.140	5.06
#04	131.47	10.11	89.89						0.260	5.08
#05	169.76	19.44	80.56	5.1	26.1	68.8			18.93	5.10
#06	188.67	19.81	80.19						21.14	5.14
#07	295.41	30.23	69.77						9.731	5.36
#08	347.54	37.35	62.65				mixed phase	$Mg_xGa_yO_z$	6.786	5.53
#09	354.29	40.8	59.2						7.335	5.58
#10	363.96	42.89	57.11	10.6	15.1	74.3			6.526	5.61
#11	365.71	45.62	54.38						9.223	5.63
#12	393.20	48.39	51.61						6.731	5.65
#13	399.65	51.09	48.91						5.684	5.67
#14	406.32	54.71	45.29						9.460	5.69
#15	426.48	56.87	43.13						7.304	5.73
#16	494.03	61.97	38.03						9.916	5.76
#17	520.15	63.88	36.12	20.7	12.5	66.8			9.339	5.78
#18	566.19	72.84	27.16	31.4	4.5	64.1	rocksalt	$Mg_xGa_{1-x}O$	32.75	5.81
#19	750.69	78.69	21.31						6.261	5.89
#20	189.19	100	0	42.5	0	57.4		MgO	1.013	

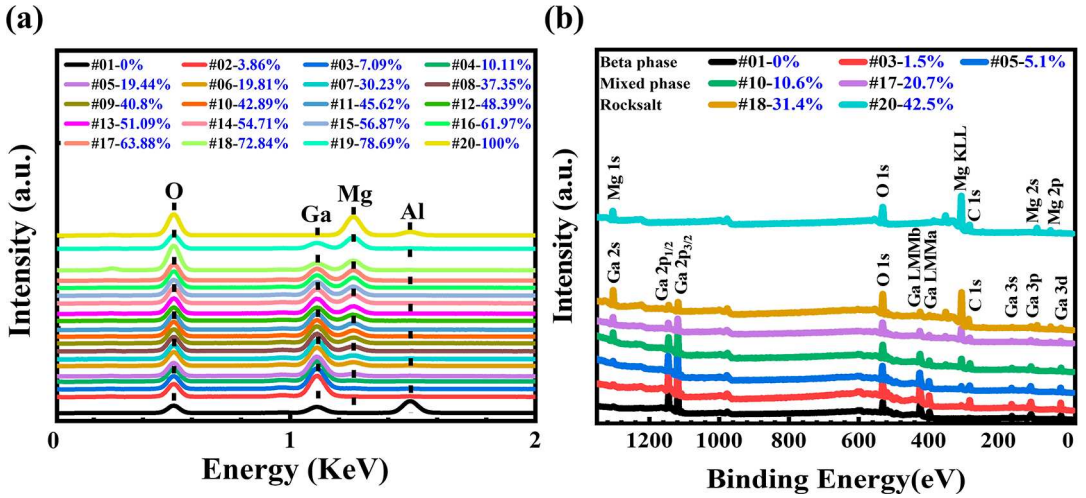

Figure 1. (a) EDX spectra of MgGaO ternary alloy thin films with the Mg atomic percent ranging from 0 to 100%. (b) XPS survey spectra of samples #01, #03, #05, #10, #17, #18, and #20.

and epitaxy relationship between MgGaO films and the c-sapphire substrate evolving with the Mg atomic percent were revealed, which provides promising potential for device applications by using high-quality band gap-tunable MgGaO thin films in the future.

2. EXPERIMENTAL SECTION

2.1. Film Growth

MgGaO thin films were grown on 2 in. c-sapphire substrates by using an RF oxygen plasma-assisted MBE system (SVT Associates, Inc.). The substrates were cleaned with Piranha solution (H_2O_2/H_2SO_4 = 3:5) at 200 °C for 20 min and rinsed by deionized water; after being dried by nitrogen gas, they were transferred to the loadlock chamber immediately. High-purity elemental Mg (4N) and Ga shots (6N) (Alfa Aesar) were used for sample growth. An 800 °C pregrowth annealing process was performed for 20 min to achieve an atomic level surface at a high vacuum of 10^{-9} Torr. The sample growth temperature was kept at 650 °C for 2 h with a 2.5 sccm flux of oxygen under a 400 W RF plasma. The Ga temperature was fixed at 750 °C by changing the Mg temperature from 390 to 460 °C; 20 MgGaO thin-film samples at various Mg atomic percents were grown, followed by a postgrowth annealing process at 700 °C under an oxygen atmosphere for 20 min.

2.2. Film Characterization

The film thickness of the samples was measured by using a Filmetrics 3D Profilometer. Surface morphologies of films were characterized by a Dimension 5000 Nanoman atomic force microscope. Mg and Ga relative atomic percents for all samples were measured by energy-dispersive X-ray (EDX) in a TESCAN Vega3 SBH scanning electron microscope instrument, and the Mg, Ga, and O relative atomic percents of several selected samples in different phases were measured by a Kratos AXIS Ultra DLD X-ray photoelectron spectroscope. Reflection high energy electron diffraction (RHEED) character-

https://doi.org/10.1021/acsaom.3c00237
ACS Appl. Opt. Mater. 2023, 1, 1670−1678

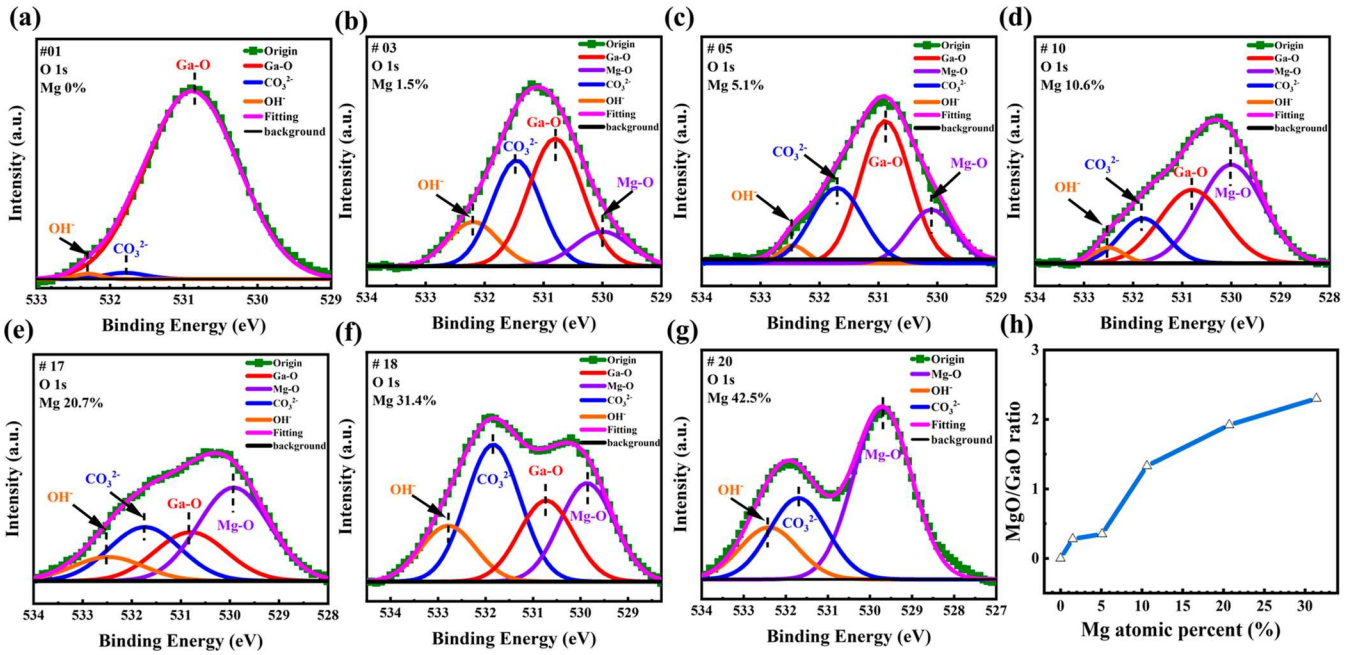

Figure 2. XPS spectra of O 1s core level spectra of MgGaO films with various Mg atomic percents (a) 0, (b) 1.5, (c) 5.1, (d) 10.6, (e) 20.7, (f) 31.4, and (g) 42.5%. (h) Mg−O to Ga−O bond ratio versus Mg atomic percent.

izations were done in ultrahigh vacuum using an electron beam with 15 keV energy. X-ray diffraction (XRD) θ–2θ, rocking curve, φ-scans, and reciprocal space mapping (RSM) measurements were used to characterize the sample structure, film quality, epitaxial relationship, and lattice parameters by using a Bruker D8 ADVANCE X-ray diffractometer and a Rigaku SmartLab X-ray diffractometer with Cu Kα (λ = 0.15405 nm) radiation at room temperature. The phonon spectra of the films were investigated by using a confocal Raman microscope equipped with a high-resolution laser with a wavelength of 532 nm and a power of 60 mW (LabRAM HR, HORIBA Scientific). Room-temperature absorption and transmittance spectra of the samples were measured by using a high-performance UV−vis−NIR spectrophotometer (Cary 5000, Agilent Inc.).

3. RESULTS AND DISCUSSION

Sample growth procedures and characterization methodologies are given in detail in the Experimental Section. Table 1 lists the characterized parameters of MgGaO samples with the Mg atomic percentage ranging from 0 to 100%. The film thickness for β-Ga_2O_3 is 117.54 nm; for rocksalt, MgO is 189.19 nm, and the thickness of MgGaO films increases from 122.17 to 750.69 nm monotonically as the Mg composition increases. Figure 1a shows the EDX spectra of all samples. O kα, Ga Lα, Mg Kα, and Al Kα are located around 0.525, 1.098, 1.253, and 1.486 keV, respectively. The Al signal is from the substrate. With more Mg incorporated in, the relative peak intensity for Ga to Mg decreases, and the Al peak intensity gradually becomes smaller due to the increasing film thickness. The relative atomic percents of Mg and Ga are listed in Table 1. X-ray photoelectron spectroscopy (XPS) analysis was also carried out to calibrate the elemental compositions of a few selected samples, including samples #01, #03, and #05 in the β phase, #10 and #17 in the mixed phase, and #18 and #20 in the rocksalt phase. Figure 1b shows XPS survey peaks of Ga 2p, Mg 2s, 2p and O 1s spectra, respectively. The spectra were calibrated with the C 1s level of 284.8 eV. Because of the limited penetration depth of X-rays and negligible photoelectrons exited from the substrate, no Al and oxygen signals from the substrate are detected in the spectra. Characteristic XPS peaks are zoomed-in and provided in the Supporting Information; as seen from Figure S1, Ga $2p_{3/2}$ and Ga $2p_{1/2}$ are located at ∼1116.4 and ∼1143.2 eV, respectively (Figure S1(a)), Mg 2s and 2p are located at ∼88.7 and ∼49.78 eV, respectively (Figure S1b), and O 1s is located at ∼531 eV (Figure S1c). Based on these peaks, the relative atomic percents of Mg, Ga, and O of these selected samples are estimated and summarized in Table 1. The Mg at. % of these 7 samples are 0, 1.5, 5.1, 10.6, 20.7, 31.4, and 42.5 at. %, respectively. As seen in Table 1, these values are different from those obtained from EDX because XPS provides a survey of all three elements Mg, Ga, and O of the thin films, while oxygen signals were excluded in the estimation of relative content of Mg and Ga in the EDX experiment due to an inevitable oxygen contribution from the substrate. Figure 2a–g shows O 1s core level spectra of these samples, in which the Shirley background was added.[34] O 1s core level spectra of these samples were deconvoluted into several fitting peaks located at ∼530.0, ∼530.84, ∼ 531.80, and ∼532.5 eV, which correspond to the binding energies of the Mg−O bond,[35] Ga−O bond,[35] and carbonate groups (CO_3^{2-}) due to absorbed carbon dioxide from atmosphere,[36,37] and surface hydroxide (OH^-),[38−40] respectively. Figure 2h shows the Mg−O/Ga−O bond peak area ratio as a function of the Mg atomic percent. The Mg−O/Ga−O bond ratio increases monotonically with Mg atomic percent, indicating that more Mg−O rather than Ga−O bonds are formed in the samples with more incorporated Mg. Besides EDX and XPS, Raman spectroscopy was also carried out as a supplementary method to confirm the Mg incorporation. Figure S2 in the Supporting Information shows Raman spectra of the samples. Compared to Ga_2O_3 (sample no. 01), optical phonon modes $A_g^{(2)-(3)}$, $A_g^{(5)}$, and $B_g^{(4)-(5)}$ of MgGaO samples change. Reduced $A_g^{(2)-(3)}$ peak intensity implies the vibration and translation of the Ga_IO_4 tetrahedral chains, reduced $A_g^{(5)}$ and enhanced $B_g^{(4)}$ modes indicate the deformation of the $Ga_{II}O_6$ octahedral chains and the translation of the Ga_IO_4

https://doi.org/10.1021/acsaom.3c00237
ACS Appl. Opt. Mater. 2023, 1, 1670−1678

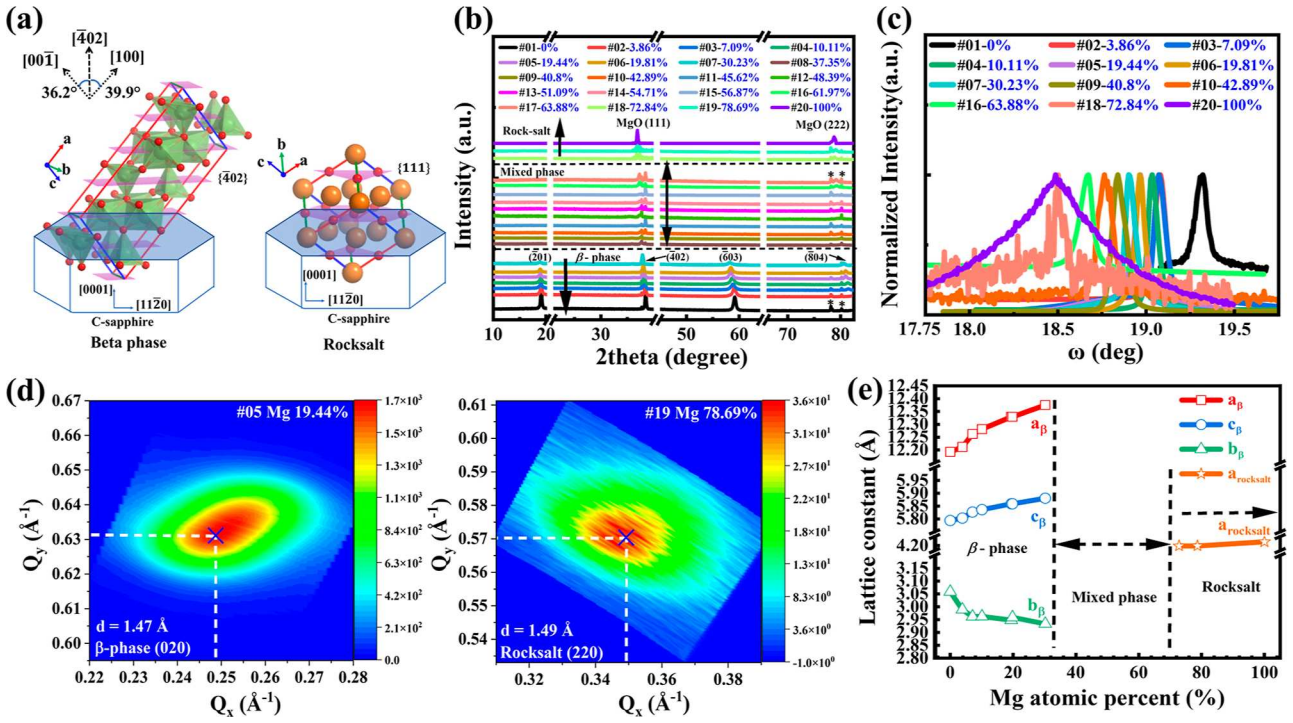

Figure 3. (a) Schematic of the MgGaO film in both β and rocksalt phases grown on c-sapphire. (b) XRD pattern of MgGaO films with various Mg atomic percents in $\theta/2\theta$ scan mode. (c) XRD rocking curves of selected MgGaO thin films. (d) In-plane reciprocal space mappings for sample #05 of the β phase of (020) and sample #19 of the rocksalt phase of (220). (e) β phase lattice constant a_β, b_β, c_β and rocksalt phase lattice constant $a_{rocksalt}$ versus Mg atomic percent.

tetrahedral chains, and smaller wavenumber of $B_g^{(5)}$ mode means the stretching and bending of Ga_1O_4 tetrahedral chains.[32,41]

Figure 3a illustrates a schematic of the MgGaO film in both β and rocksalt phases grown on c-sapphire. The vertical growth orientations are $\langle\bar{2}01\rangle_{\beta\text{-phase}} \parallel \langle 0001\rangle_{\text{C-sapphire}}$ and $\langle 111\rangle_{\text{rocksalt}} \parallel \langle 0001\rangle_{\text{C-sapphire}}$, respectively. Figure 3b shows the XRD pattern in $\theta/2\theta$ scan mode of all MgGaO samples. For Mg at. % ranging from 0 to 30.23%, MgGaO samples are in the β phase, and four typical diffraction peaks located at ~19.12, 38.50, 59.14, and 82.37° correspond to the β phases of ($\bar{2}$01), ($\bar{4}$02), ($\bar{6}$03), and ($\bar{8}$04), respectively, implying a clear monoclinic structure. In these β-phase MgGaO samples, divalent Mg substitutes trivalent Ga sites;[32] thus, the chemical formula can be written as $(Mg_xGa_{1-x})_2O_3$ (Table 1). For example, the chemical formula of sample #02 is $(Mg_{0.0386}Ga_{0.9614})_2O_3$ or roughly $(Mg_{0.04}Ga_{0.96})_2O_3$. With more Mg incorporated in MgGaO samples, the diffraction angles exhibit an obvious decrease due to a larger Mg ionic radius (0.72 Å) than that of Ga (0.62 Å). For Mg at. % ranging from 72.84 to 100%, MgGaO samples are in the pure rocksalt phase, and two typical diffraction peaks located at ~36.9 and 78.5° correspond to the rocksalt phase of (111) and (222), respectively.[42] In these rocksalt MgGaO samples, the Ga atom is assumed to substitute the Mg atom site in the lattice; thus, the chemical formula may be written as $Mg_xGa_{1-x}O$. Taking sample #18 for example, the chemical formula is $Mg_{0.7284}Ga_{0.2716}O$ or roughly $Mg_{0.73}Ga_{0.27}O$. For Mg at. % ranging from 37.35 to 63.88%, MgGaO samples are in the mixed phase since both ($\bar{4}$02) and ($\bar{8}$04) of the β phase and (111) and (222) of the rocksalt phase coexist in the XRD pattern. Due to the mixed phase nature of the film in this region, the preferred way to write the chemical formula is in the form of $Mg_xGa_yO_z$, where x, y, and z are the relative atomic percent among Mg, Ga, and O elements. Taking sample #10 as an example, the chemical formula is $Mg_{0.314}Ga_{0.045}O_{0.641}$ or roughly $Mg_{0.31}Ga_{0.05}O_{0.64}$. Based on the $\theta/2\theta$ scan results, β-MgGaO and rocksalt MgGaO grown on the c-sapphire {0001} plane are highly {$\bar{2}$01} and {111} oriented, respectively. In addition, no MgGaO thin films in the β and rocksalt mixed phase regime exhibit a spinel phase as existed in $MgGa_2O_4$, $MgAl_2O_4$, and other spinel oxides. The growth of spinel MgGaO may be achieved on sapphire substrates with suitable orientation or under suitable growth conditions, which needs further studies. Figure 3c shows normalized XRD rocking curves of the selected 12 samples among the three phase regions. The full width at half-maximum (fwhm) of samples #01−#07 in the β phase are 0.0831, 0.0792, 0.0789, 0.0716, 0.0919, 0.0796, and 0.0793°, samples #09−#10, #16 in the mixed phase are 0.0933, 0.1000, and 0.0960°, and samples #18, #20 in the rocksalt phase are 0.0988° and 0.5014°, respectively. These very small fwhm values suggest that our β phase films are of very high quality.[43]

To reveal how the lattice parameters of MgGaO thin films change with Mg atomic percent, besides $\theta/2\theta$ scan, in-plane RSM was measured for films in both the β phase and rocksalt phase. As for the monoclinic structure of Ga_2O_3, the reference lattice constants a_β, b_β, c_β, β angle between a and c axes and $d_{(\bar{4}02)}$ are ~12.020 Å, ~3.04 Å, ~5.799 Å, 103.7°, and 2.34 Å, respectively. Assuming that the monoclinic structure is stable after Mg is incorporated, as shown in Figure 3a, the angle between orientations [$\bar{4}$02] and [00$\bar{1}$] and between orientations [$\bar{4}$02] and [100] can be calculated as ~36.2 and ~39.9°, respectively. Therefore, lattice constants a_β and c_β can be calculated as follows

https://doi.org/10.1021/acsaom.3c00237
ACS Appl. Opt. Mater. 2023, 1, 1670−1678

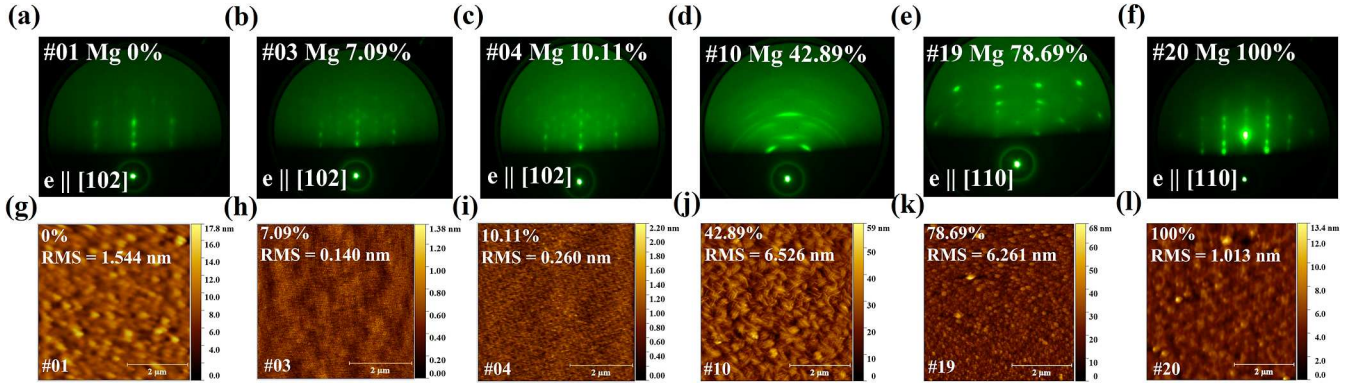

Figure 4. (a–f) RHEED patterns and (g–l) AFM images of MgGaO ternary alloy thin films at different Mg atomic percents 0, 7.09, 10.11, 42.89, 42.89, and 100%, respectively.

$$a_\beta = 4 \times \frac{d_{(\bar{4}02)}}{\cos(39.9^\circ)} \quad (1)$$

$$c_\beta = 2 \times \frac{d_{(\bar{4}02)}}{\cos(36.2^\circ)} \quad (2)$$

According to Bragg's law, the β-phase $(\bar{4}02)$ interplanar distance $d_{(\bar{4}02)}$ can be estimated from $\theta/2\theta$ scans. Based on the above equations, lattice constants a_β and c_β were calculated and are listed in Table S1 of the Supporting Information. For pure rocksalt samples, interplanar distance $d_{(111)}$ can be estimated from $\theta/2\theta$ scans and the lattice constant $a_{rocksalt}$ can be calculated as $\sqrt{3}\,d_{(111)}$, which is also listed in Table S1 of the Supporting Information; for example, it is ~4.2 Å for sample #20. As an alternative method to the $\theta/2\theta$ scan for the estimation of the out-of-plane d-spacing, the out-of-plane RSM was measured (Figure S3a–g, Supporting Information). It shows that the calculated lattice constant values by two methods are almost the same (Figure S3h, Supporting Information). Figure 3d shows an example of in-plane reciprocal space mappings for the (020) plane of β phase sample #05 and (220) plane of rocksalt phase sample #19, respectively. Figure S4 in the Supporting Information shows RSM for other samples. According to β-Ga_2O_3 PDF 01-087-1901, the reference d-spacing value of the (020) plane is ~1.52 Å, and the β phase lattice constant b_β is twice that of $d_{(020)}$, which is ~3.04 Å. According to MgO PDF 00-004-0829, the reference d-spacing value of the (220) plane is ~1.48 Å, and the rocksalt phase lattice constant $a_{rocksalt}$ is $2\sqrt{2}\,d_{(220)}$, which is ~4.2 Å. Based on these mathematical relationships, the lattice constants b_β and $a_{rocksalt}$ of respective MgGaO samples are calculated from the in-plane RSM data and listed in Table S1 of the Supporting Information. For rocksalt samples, the lattice constant values calculated from both $\theta/2\theta$ and in-plane RSM scans are the same, indicating the cubic structure. Figure 3e shows the lattice constants as a function of the Mg atomic percent. In β-phase MgGaO samples, the parameters a_β and c_β increase, while b_β decreases with the increase of Mg atom % compared to that of the reference sample β-Ga_2O_3. In rocksalt phase MgGaO samples, the lattice constant $a_{rocksalt}$ changes only slightly as Mg increases compared to that of the reference sample MgO.

To understand the epitaxial relationship between MgGaO films and the c-sapphire substrate, the RHEED was measured. Figure 4a–f shows RHEED patterns of MgGaO thin films with Mg at. % of 0%, 7.09%, 10.11% in the β phase, 42.89% in the mixed phase, and 78.69% and 100% in the rocksalt phase, respectively. The streaky-like patterns of the β-phase $\{\bar{2}01\}$ plane along [102] azimuth (Figure 4a–c) and along [010] azimuth (Figure S5a–c, Supporting Information) indicate high crystallinity of the films, which are similar to those RHEED patterns obtained from β-Ga_2O_3.[44,45] Based on the RHEED patterns, in-plane lattice constants $a_{\parallel[102]}$ and $a_{\parallel[010]}$, which are the distance between (010) planes and between (102) planes as illustrated in a schematic of the atom arrangement of $(\bar{2}01)$ surface (Figure S6a in the Supporting Information), were calculated as ~2.98 and 5.06 Å for sample #01, ~2.88 and 5.11 Å for sample #03, and ~2.84 and 5.17 Å for sample #04, respectively. These numbers are analogous to ~3.04 and 4.96 Å of the reported in-plane lattice constants of β-Ga_2O_3.[46] These surface lattice parameters can be used to estimate the lattice constants of unit cells a_β, b_β, and c_β of these β-phase samples. First, b_β is equal to $a_{\parallel[102]}$. Then, a schematic showing the side-view of the unit cell in Figure S6b of the Supporting Information is used to calculate a_β and c_β. Since β-phase samples have a surface plane of $(\bar{2}01)$, the lateral length along the [102] direction within the unit cell is generally expressed as $K \times a_{\parallel[010]}$, where K is a multiple and can only take integer or half-integer as can be inferred from surface atom arrangement on the $(\bar{2}01)$ plane along the [102] direction (designated as $(\bar{2}01)[102]$) in Figure S6a in the Supporting Information. The projections of $a_\beta/2$ and c_β onto $\langle\bar{2}01\rangle$ are equal, while $K \times a_{\parallel[010]}$ equals the sum of projections of $a_\beta/2$ and c_β onto $(\bar{2}01)[102]$. These relationships can be written as follows

$$\frac{a_\beta}{2} \times \cos(39.9^\circ) = c_\beta \times \cos(36.2^\circ) \quad (3)$$

$$\frac{a_\beta}{2} \times \sin(39.9^\circ) + c_\beta \times \sin(36.2^\circ) = K \times a_{\parallel[010]} \quad (4)$$

According to eq 3, $c_\beta = a_\beta/2.104$, which is compatible with the result of eq 1/eq 2. After replacing c_β with a_β in eq 4, $a_\beta = 1.663 \times K \times a_{\parallel[010]}$. Taking sample #01 as an example, $a_{\parallel[010]} = 5.06$ Å, only when K equals ~1.5, a_β and c_β can be calculated as 12.62 and 6 Å, which would be close to the Ga_2O_3 reference lattice constant. With this method, the lattice constant values of these samples are calculated and listed in Table S2 of the Supporting Information, which are in good agreement with that obtained by XRD characterizations. These numbers indicate that the film $\{\bar{2}01\}$ plane is compressed along the [010] orientation and stretched along the [102] orientation

https://doi.org/10.1021/acsaom.3c00237
ACS Appl. Opt. Mater. 2023, 1, 1670–1678

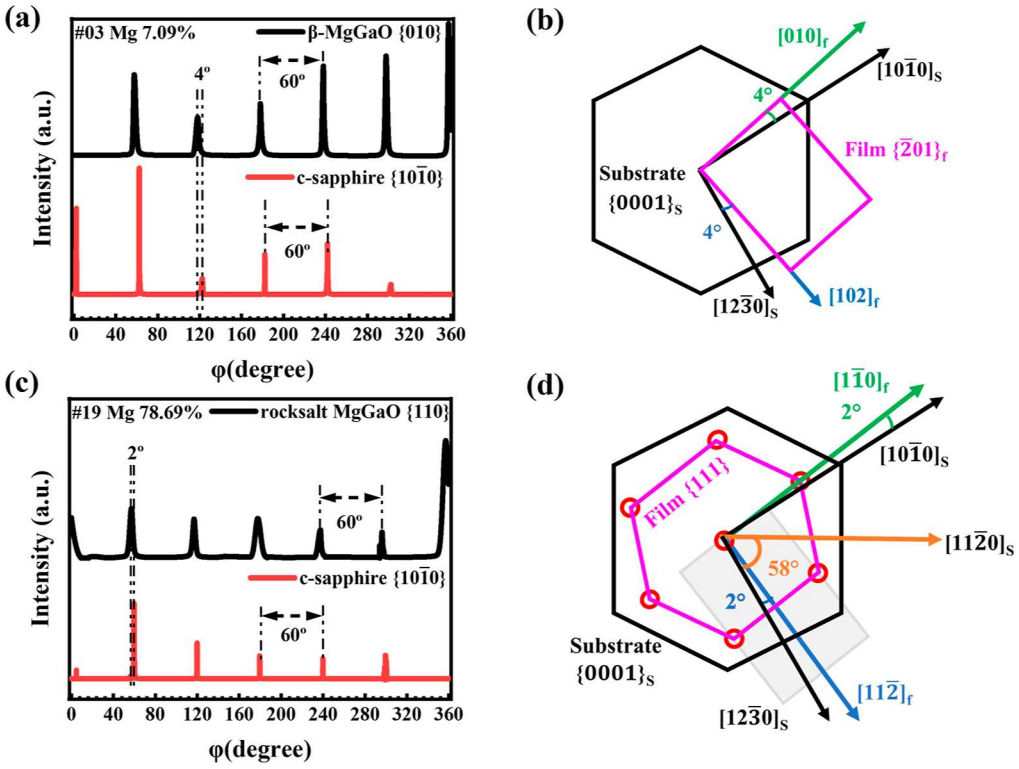

Figure 5. (a) φ-scan patterns of β-MgGaO {010} and c-sapphire {10$\bar{1}$0} planes. (b) Schematic diagram of the epitaxial relationship for β-MgGaO and on a c-sapphire substrate. (c) φ-Scan patterns of rocksalt MgGaO {110} and c-sapphire {10$\bar{1}$0} planes. (d) Schematic of the epitaxial relationship of rocksalt MgGaO on a c-sapphire substrate.

with the increase of Mg at. %, which is compatible with the decrease of b_β and the increase of a_β and c_β in Figure 3e. As seen in Figure 4d, the RHEED pattern of sample #10 in the mixed phase exhibits the Debye ring, which indicates the polycrystal nature.[47] Figure 4e,f shows RHEED patterns of the rocksalt phase {111} plane along [1$\bar{1}$0] azimuth of samples #19 and #20, respectively. The in-plane lattice constant $a_{\parallel[1\bar{1}0]}$, namely, the distance between (11$\bar{2}$) planes, was calculated as ∼5.20 and ∼5.12 Å for samples #19 and #20, respectively. Based on the rocksalt structure (Figure 3a), the lattice constant $a_{rocksalt}$ of MgGaO unit cell for samples #19 and #20 was calculated as $a_{\parallel[1\bar{1}0]}/(\sqrt{3/2})$, which is 4.25 and 4.18 Å, respectively (Table S2, Supporting Information). These are also in good agreement with the results obtained by XRD. It is noted that most RHEED patterns are not exactly streaky lines but contain spots, indicating the possible formation of islands in real space.[48] The atomic force microscopy (AFM) 5 μm × 5 μm images of corresponding samples are shown in Figure 4g–l, and the surface morphology of other samples was characterized by AFM as well (Figure S7, Supporting Information). The root-mean-square roughness of all samples, which is also listed in Table 1, agrees with the RHEED results.

To further study the in-plane epitaxial relationship of MgGaO thin films in both β and rocksalt phases on the c-sapphire substrate, XRD φ-scans were measured. Figure 5a shows φ-scan patterns of β-MgGaO {010} of sample no. 03 at a position of the detector 2theta_chi = 60.961° and c-sapphire {10$\bar{1}$0} (2theta_chi = 68.212°) (PDF 00-046-1212). The φ-scan patterns of other β-phase samples #01 and #04 are shown in Figure S8a,b in the Supporting Information. Similar to β-Ga_2O_3 on the c-sapphire substrate,[44,46,49] six peaks are observed and separated by 60° for both φ-scan patterns of the substrate and film, indicating the 6-fold rotational symmetry for films growing on the c-sapphire {0001} plane in the [0001] orientation. Compared with the 1.8° rotation between $\langle 102\rangle_f$ and $\langle 10\bar{1}0\rangle_s$,[46] where the subscripts "f" and "s" mean the film and c-sapphire substrate, respectively, there is a 4° rotation between $\langle 010\rangle_f$ and $\langle 10\bar{1}0\rangle_s$. Besides, $\{\bar{2}01\}_{\beta\text{-phase}}$ $\langle 010\rangle_f \perp \{\bar{2}01\}_{\beta\text{-phase}}$ $\langle 102\rangle_f$, and $\{0001\}_s$ $\langle 10\bar{1}0\rangle_s \perp \{0001\}_s$ $\langle 12\bar{3}0\rangle_s$; therefore, the epitaxy relationship between the film and substrate in the β phase is $\{\bar{2}01\}_{\beta\text{-phase}}$ $\langle 010\rangle_f \parallel \{0001\}_s$ $\langle 10\bar{1}0\rangle_s$, $\{\bar{2}01\}_{\beta\text{-phase}}$ $\langle 102\rangle_f \parallel \{0001\}_s$ $\langle 12\bar{3}0\rangle_s$ with a 4° rotation, which is illustrated in Figure 5b. Figure 5c shows φ-scan patterns of rocksalt MgGaO {110} of sample #19 at 2theta_chi = 62.304° and c-sapphire {10$\bar{1}$0} (2theta_chi = 68.212°). φ-scan patterns of similar rocksalt samples #18 and #20 are shown in Figure S8(c)-(d) in the Supporting Information. Six diffraction peaks with 60° separation show up similar to β-MgGaO; however, there is a 2° rotation between $\langle 110\rangle_f$ and $\langle 10\bar{1}0\rangle_s$. Besides, $\{111\}_{rocksalt}[1\bar{1}0]_f \perp \{111\}_{rocksalt}[11\bar{2}]_f$. Thus, the epitaxy relationship between the film and substrate is $\{111\}_{rocksalt}$ $\langle 110\rangle_f \parallel \{0001\}_s$ $\langle 10\bar{1}0\rangle_s$, and $\{111\}_{rocksalt}$ $\langle 11\bar{2}\rangle_f \parallel \{0001\}_s$ $\langle 12\bar{3}0\rangle_s$ with a 2° rotation, which is illustrated in Figure 5d. The arrangement of the oxygen atom in red circles in the rocksalt {111} plane forms the hexagonal shape. Due to $\langle 110\rangle_f \parallel \langle 10\bar{1}0\rangle_s$ with a 2° rotation, the angle between $\langle 11\bar{2}\rangle_f$ and $\langle 21\bar{3}0\rangle_s$ is around 58°. In other words, the {111} plane of films rotates almost 60° matching the {0001} plane of the substrate.

Although β and rocksalt phases belong to the monoclinic and cubic systems, respectively, the arrangement of the oxygen atoms in the β phase $\{\bar{2}01\}$ plane and rocksalt {111} plane is hexagonal, which is similar to the arrangement of oxygen atoms in the c-sapphire {0001} plane. Referring to the three PDF

https://doi.org/10.1021/acsaom.3c00237
ACS Appl. Opt. Mater. 2023, 1, 1670−1678

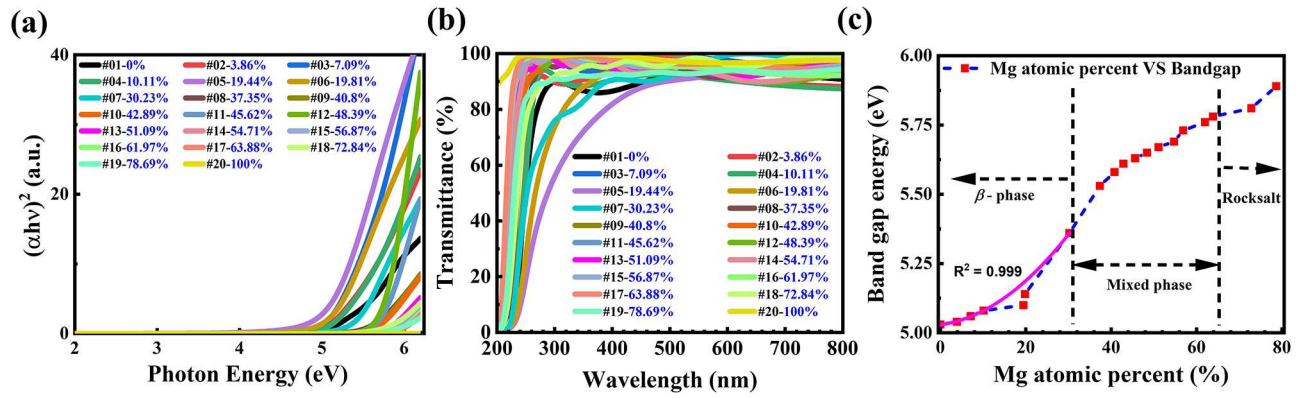

Figure 6. (a) Tauc plot of the absorption spectra. (b) Transmittance spectra of MgGaO thin films with Mg atomic percent ranging from 0 to 100%. (c) Band gap versus Mg atomic percent of MgGaO samples.

cards mentioned above, the atom arrangement of the c-sapphire {0001} plane, β phase $\{\bar{2}01\}$ plane, and rocksalt {111} plane is illustrated (Figure S9, Supporting Information). The O−O bond length along the $\{0001\}_s[01\bar{1}0]$ orientation is ∼2.725 Å, $\{\bar{2}01\}_{\beta\text{-phase}}[010]$ orientation is ∼2.782 Å, and $\{111\}_{\text{rocksalt}}$ [110] orientation is ∼2.97 Å. It should be mentioned that the O−O bond length along the $\{111\}_{\text{rocksalt}}$ [110] orientation is equal to $\sqrt{2}$ times the Mg−O bond length. Because of the similar hexagonal oxygen atom arrangement with similar bond lengths, both β phase and rocksalt phase MgGaO can be readily epitaxial on the c-sapphire substrate.[49]

Band gaps of MgGaO samples were studied by absorption spectroscopy. Figure 6a shows a Tauc plot of the absorption spectra of all samples. Since direct band gaps of ∼5.0 eV for β-Ga_2O_3[50−52] and ∼7.8 eV for MgO[53−55] were reported, their mixture MgGaO ternary alloys are assumed to possess the direct band gap property. The Tauc equation for semiconductors with direct band gaps is expressed as

$$(\alpha h\upsilon)^2 = A(h\upsilon - E_g) \tag{5}$$

where α is the absorption coefficient, $h\upsilon$ is energy, and A is a proportionality constant. By extrapolating the linear segment of absorption spectra to intersect the $h\upsilon$-axis with a fitting straight line, the band gap was extracted and is listed in Table 1. The maximum value of the tuned band gap is ∼5.89 eV for sample #19, which has Mg and Ga compositions of ∼79 and 21%, respectively. However, the band gap of sample #20 MgO cannot be measured due to the wavelength limitations (200 nm minimum) of the UV−vis−NIR spectrophotometer, although it is presumably equal to 7.8 eV. The transmittance of these samples was also measured using the same spectrophotometer, as shown in Figure 6b. ∼90% transmittance of light at the visible region was observed across the spectrum for all samples. Figure 6c shows the band gap as a function of Mg composition in the MgGaO films. The band gap increases monotonically with the increase of Mg at. %.

To deduce the relationship between the band gap and Mg composition, a polynomial model was used to fit band gap versus Mg at. %,[56] which is illustrated as the solid line in Figure 6c. Due to the mixed phase crystal structure, and the limited data points in rocksalt regions, fitting was done only for the beta phase, which can be written as $E_g(x) = E_g(0) + Ax + Bx^2$, where E_g (0) is the band gap of Ga_2O_3, A and B are constant, and x is the Mg atomic percent. The fitting yields the following formula

$$E_g(x) = 5.03 + 0.21x + 2.94x^2 \tag{6}$$

Taking sample #07 as an example, where Mg at. % is 30.23%, $E_g(x) = 5.03 + 0.21 \times 30.23\% + 2.94(30.23\%)^2 = 5.36$ eV, which is equal to the experimental value of 5.36 eV.

4. CONCLUSIONS

We systematically investigated the phase transition and band gap engineering in UWBG MgGaO thin films. Twenty samples with Mg at. % ranging from 0 to 100% were grown by MBE. Phase transformation from the β phase to the mixed phase and finally to the rocksalt phase was benchmarked. When the Mg atom % is between 0 and 30.23%, MaGaO is the pure β phase; when the Mg atom % is between 37.35 and 63.88%, MgGaO is a mixture of β and rocksalt phases; when the Mg atom % is larger than 72.84%, MaGaO films are the pure rocksalt phase. Meanwhile, the lattice parameter and band gaps of MgGaO thin films were quantified, and the epitaxial relationship between the film in both β phase and rocksalt phase and substrate was determined. This work shows that the MgGaO ternary alloy is an alternatively viable candidate for band gap-increasing band gap engineering of Ga_2O_3; therefore, it is promising for UWBG Ga_2O_3-based device applications.

■ ASSOCIATED CONTENT

Supporting Information

The Supporting Information is available free of charge at https://pubs.acs.org/doi/10.1021/acsaom.3c00237.

XPS details of Ga 2s, Mg 2s, 2p and O 1s spectra; Raman spectra; out-of-plane reciprocal spacing mapping; in-plane reciprocal spacing mapping; RHEED images; schematic of calculation for a_β and c_β based on RHEED; AFM images; XRD φ-scans spectra; atom arrangement of c-sapphire {0001}, β-Ga_2O_3 $\{\bar{2}01\}$, and MgO {111} planes; XRD peak positions, fwhm, d-spacing, and lattice parameters; and RHEED parameter and lattice constant (PDF)

■ AUTHOR INFORMATION

Corresponding Author

Jianlin Liu − *Department of Electrical and Computer Engineering, University of California, Riverside, California 92521, United States;* orcid.org/0000-0001-6513-0867; Phone: 1-9518277131; Email: jianlin@ece.ucr.edu; Fax: 1-9518272425

https://doi.org/10.1021/acsaom.3c00237
ACS Appl. Opt. Mater. 2023, 1, 1670−1678

Authors

Tianchen Yang − *Department of Electrical and Computer Engineering, University of California, Riverside, California 92521, United States;* orcid.org/0000-0002-0991-471X

Chengyun Shou − *Department of Electrical and Computer Engineering, University of California, Riverside, California 92521, United States*

Abdullah Almujtabi − *Department of Electrical and Computer Engineering, University of California, Riverside, California 92521, United States*

Jason Tran − *Department of Physics and Astronomy, University of California, Riverside, California 92521, United States*

Qiyin Lin − *Irvine Materials Research Institute (IMRI), University of California, Irvine, California 92697, United States*

Yuan Li − *Department of Electrical and Computer Engineering, University of California, Riverside, California 92521, United States*

Quazi Sanjid Mahmud − *Department of Electrical and Computer Engineering, University of California, Riverside, California 92521, United States*

Peng Wei − *Department of Physics and Astronomy, University of California, Riverside, California 92521, United States;* orcid.org/0000-0003-2289-6007

Complete contact information is available at: https://pubs.acs.org/10.1021/acsaom.3c00237

Notes

The authors declare no competing financial interest.

■ ACKNOWLEDGMENTS

This work was supported by the National Science Foundation (ECCS-2105566) and the Air Force Office of Scientific Research under DURIP award number FA9550-22-1-0505. The authors acknowledge the use of facilities and instrumentation at the UC Irvine Materials Research Institute (IMRI), which is supported in part by the National Science Foundation through the UC Irvine Materials Research Science and Engineering Center (DMR-2011967) and the use of XPS instruments at UC Riverside, which is supported by the National Science Foundation (DMR-0958796). J.T. and P.W. would like to acknowledge NSF under award NSF CAREER-2046648.

■ REFERENCES

(1) Casady, J. B.; Johnson, R. W. Status of Silicon Carbide (SiC) as a Wide-Bandgap Semiconductor for High-Temperature Applications: A Review. *Solid-State Electron.* **1996**, *39* (10), 1409−1422.

(2) Kim, M.; Seo, J.-H.; Singisetti, U.; Ma, Z. Recent Advances in Free-Standing Single Crystalline Wide Band-Gap Semiconductors and Their Applications: GaN, SiC, ZnO, β-Ga_2O_3, and Diamond. *J. Mater. Chem. C* **2017**, *5* (33), 8338−8354.

(3) Monroy, E.; Omns, F.; Calle, F. Wide-Bandgap Semiconductor Ultraviolet Photodetectors. *Semicond. Sci. Technol.* **2003**, *18* (4), R33−R51.

(4) Tsao, J. Y.; Chowdhury, S.; Hollis, M. A.; Jena, D.; Johnson, N. M.; Jones, K. A.; Kaplar, R. J.; Rajan, S.; Van de Walle, C. G.; Bellotti, E.; Chua, C. L.; Collazo, R.; Coltrin, M. E.; Cooper, J. A.; Evans, K. R.; Graham, S.; Grotjohn, T. A.; Heller, E. R.; Higashiwaki, M.; Islam, M. S.; Juodawlkis, P. W.; Khan, M. A.; Koehler, A. D.; Leach, J. H.; Mishra, U. K.; Nemanich, R. J.; Pilawa-Podgurski, R. C. N.; Shealy, J. B.; Sitar, Z.; Tadjer, M. J.; Witulski, A. F.; Wraback, M.; Simmons, J. A. Ultrawide-Bandgap Semiconductors: Research Opportunities and Challenges. *Adv. Electron. Mater.* **2018**, *4* (1), 1600501.

(5) Xie, C.; Lu, X.-T.; Tong, X.-W.; Zhang, Z.-X.; Liang, F.-X.; Liang, L.; Luo, L.-B.; Wu, Y.-C. Recent Progress in Solar-Blind Deep-Ultraviolet Photodetectors Based on Inorganic Ultrawide Bandgap Semiconductors. *Adv. Funct. Mater.* **2019**, *29* (9), 1806006.

(6) Pearton, S. J.; Yang, J.; Cary, P. H.; Ren, F.; Kim, J.; Tadjer, M. J.; Mastro, M. A. A Review of Ga_2O_3 Materials, Processing, and Devices. *Applied Physics Reviews* **2018**, *5* (1), 011301.

(7) Oh, S.; Kim, C.-K.; Kim, J. High Responsivity β-Ga_2O_3 Metal-Semiconductor-Metal Solar-Blind Photodetectors with Ultraviolet Transparent Graphene Electrodes. *ACS Photonics* **2018**, *5* (3), 1123−1128.

(8) Qin, Y.; Li, L.; Zhao, X.; Tompa, G. S.; Dong, H.; Jian, G.; He, Q.; Tan, P.; Hou, X.; Zhang, Z.; Yu, S.; Sun, H.; Xu, G.; Miao, X.; Xue, K.; Long, S.; Liu, M. Metal-Semiconductor-Metal ϵ-Ga_2O_3 Solar-Blind Photodetectors with a Record-High Responsivity Rejection Ratio and Their Gain Mechanism. *ACS Photonics* **2020**, *7* (3), 812−820.

(9) Chen, X.; Ren, F.; Gu, S.; Ye, J. Review of Gallium-Oxide-Based Solar-Blind Ultraviolet Photodetectors. *Photon. Res.* **2019**, *7* (4), 381.

(10) Zhao, B.; Wang, F.; Chen, H.; Zheng, L.; Su, L.; Zhao, D.; Fang, X. An Ultrahigh Responsivity (9.7 MA W^{-1}) Self-Powered Solar-Blind Photodetector Based on Individual ZnO - Ga_2O_3 Heterostructures. *Adv. Funct. Mater.* **2017**, *27* (17), 1700264.

(11) Liu, Z.; Yamazaki, T.; Shen, Y.; Kikuta, T.; Nakatani, N.; Li, Y. O_2 and CO Sensing of Ga_2O_3 Multiple Nanowire Gas Sensors. *Sens. Actuators, B* **2008**, *129* (2), 666−670.

(12) Lampe, U.; Fleischer, M.; Meixner, H. Lambda Measurement with Ga_2O_3. *Sens. Actuators, B* **1994**, *17* (3), 187−196.

(13) Sharma, S.; Zeng, K.; Saha, S.; Singisetti, U. Field-Plated Lateral Ga_2O_3 MOSFETs With Polymer Passivation and 8.03 KV Breakdown Voltage. *IEEE Electron Device Lett.* **2020**, *41* (6), 836−839.

(14) Higashiwaki, M.; Sasaki, K.; Kamimura, T.; Hoi Wong, M.; Krishnamurthy, D.; Kuramata, A.; Masui, T.; Yamakoshi, S. Depletion-Mode Ga_2O_3 Metal-Oxide-Semiconductor Field-Effect Transistors on β- Ga_2O_3 (010) Substrates and Temperature Dependence of Their Device Characteristics. *Appl. Phys. Lett.* **2013**, *103* (12), 123511.

(15) Zeng, K.; Vaidya, A.; Singisetti, U. 1.85 KV Breakdown Voltage in Lateral Field-Plated Ga_2O_3 MOSFETs. *IEEE Electron Device Lett.* **2018**, *39* (9), 1385−1388.

(16) Chen, Y.; Lu, Y.; Yang, X.; Li, S.; Li, K.; Chen, X.; Xu, Z.; Zang, J.; Shan, C. Bandgap Engineering of Gallium Oxides by Crystalline Disorder. *Mater. Today Phys.* **2021**, *18*, 100369.

(17) Zhang, F.; Saito, K.; Tanaka, T.; Nishio, M.; Guo, Q. Wide Bandgap Engineering of $(GaIn)_2O_3$ Films. *Solid State Commun.* **2014**, *186*, 28−31.

(18) Zhang, F.; Saito, K.; Tanaka, T.; Nishio, M.; Guo, Q. Thermal Annealing Impact on Crystal Quality of $(GaIn)_2O_3$ Alloys. *J. Alloys Compd.* **2014**, *614*, 173−176.

(19) Oshima, T.; Fujita, S. Properties of Ga_2O_3-Based $(In_xGa_{1-x})_2O_3$ Alloy Thin Films Grown by Molecular Beam Epitaxy. *Phys. Status Solidi C* **2008**, *5* (9), 3113−3115.

(20) Hamberg, I.; Granqvist, C. G.; Berggren, K.-F.; Sernelius, B. E.; Engström, L. Band-Gap Widening in Heavily Sn-Doped In_2O_3. *Phys. Rev. B* **1984**, *30* (6), 3240−3249.

(21) Zhang, J.; Shi, J.; Qi, D.-C.; Chen, L.; Zhang, K. H. L. Recent Progress on the Electronic Structure, Defect, and Doping Properties of Ga_2O_3. *APL Mater.* **2020**, *8* (2), 020906.

(22) Wang, D.; Ge, K.; Meng, D.; Chen, Z. P-Type β-Ga_2O_3 Films Were Prepared by Zn-Doping Using RF Magnetron Sputtering. *Mater. Lett.* **2023**, *330*, 133251.

(23) Shen, Y.-S.; Wang, W.-K.; Horng, R.-H. Characterizations of Metal-Oxide-Semiconductor Field-Effect Transistors of ZnGaO Grown on Sapphire Substrate. *IEEE J. Electron Devices Soc.* **2017**, *5* (2), 112−116.

(24) Singh, A. K.; Yen, C.-C.; Chang, K.-P.; Wuu, D.-S. Structural and Photoluminescence Properties of Co-Sputtered p-Type Zn-

Doped β-Ga_2O_3 Thin Films on Sapphire Substrates. *J. Lumin.* **2023**, *260*, 119836.
(25) Alema, F.; Hertog, B.; Ledyaev, O.; Volovik, D.; Thoma, G.; Miller, R.; Osinsky, A.; Mukhopadhyay, P.; Bakhshi, S.; Ali, H.; Schoenfeld, W. V. Solar Blind Photodetector Based on Epitaxial Zinc Doped Ga_2O_3 Thin Film. *Phys. Status Solidi A* **2017**, *214* (5), 1600688.
(26) Hatipoglu, I.; Mukhopadhyay, P.; Alema, F.; Sakthivel, T. S.; Seal, S.; Osinsky, A.; Schoenfeld, W. V. Tuning the responsivity of monoclinic $({In}_x{Ga}_{1-x})_2{O}_3$ solar-blind photodetectors grown by metal organic chemical vapor deposition. *J. Phys. D: Appl. Phys.* **2020**, *53* (45), 454001.
(27) Cheng, Y.-C.; Chang, S.-P.; Yang, C.-P.; Chang, S.-J. Integration of Bandgap-Engineered Double-Stacked Channel Layers with Nitrogen Doping for High-Performance InGaO TFTs. *Appl. Phys. Lett.* **2019**, *114* (19), 192102.
(28) Shen, Y.-S.; Wang, W.-K.; Horng, R.-H. Characterizations of Metal-Oxide-Semiconductor Field-Effect Transistors of ZnGaO Grown on Sapphire Substrate. *IEEE J. Electron Devices Soc.* **2017**, *5* (2), 112−116.
(29) Bhuiyan, A. F. M. A. U.; Feng, Z.; Johnson, J. M.; Huang, H.-L.; Hwang, J.; Zhao, H. MOCVD Growth of β-Phase $(Al_xGa_{1-x})_2O_3$ on (01) β-Ga_2O_3 Substrates. *Appl. Phys. Lett.* **2020**, *117* (14), 142107.
(30) Zhang, F.; Saito, K.; Tanaka, T.; Nishio, M.; Arita, M.; Guo, Q. Wide Bandgap Engineering of $(AlGa)_2O_3$ Films. *Appl. Phys. Lett.* **2014**, *105* (16), 162107.
(31) Miller, R.; Alema, F.; Osinsky, A. Epitaxial β-Ga_2O_3 and β-$(Al_xGa_{1-x})_2O_3$/β-Ga_2O_3 Heterostructures Growth for Power Electronics. *IEEE Trans. Semicond. Manuf.* **2018**, *31* (4), 467−474.
(32) Yang, T.; Shou, C.; Xu, L.; Tran, J.; He, Y.; Li, Y.; Wei, P.; Liu, J. Metal-Semiconductor-Metal Photodetectors Based on β-MgGaO Thin Films. *ACS Appl. Electron. Mater.* **2023**, *5* (4), 2122−2130.
(33) Shou, C.; Yang, T.; Almujtabi, A.; Yang, T.; Li, Y.; Mahmud, Q. S.; Xu, M.; Zheng, J.-G.; Liu, J. Improving Crystal Quality of β-Phase MgGaO Thin Films by Using Low-Temperature Homo-Buffer Layer. *Appl. Phys. Lett.* **2023**, *122* (21), 212101.
(34) Zhang, N.; Liu, H.; Sai, Q.; Shao, C.; Xia, C.; Wan, L.; Feng, Z. C.; Mohamed, H. F. Structural and Electronic Characteristics of Fe-Doped β-Ga_2O_3 Single Crystals and the Annealing Effects. *J. Mater. Sci.* **2021**, *56* (23), 13178−13189.
(35) Chu, S.-Y.; Yeh, T.-H.; Lee, C.-T.; Lee, H.-Y. Mg-Doped Beta-Ga2O3 Films Deposited by Plasma-Enhanced Atomic Layer Deposition System for Metal-Semiconductor-Metal Ultraviolet C Photodetectors. *Mater. Sci. Semicond. Process.* **2022**, *142*, 106471.
(36) Gao, P.; Tian, X.; Yang, C.; Zhou, Z.; Li, Y.; Wang, Y.; Komarneni, S. Fabrication, Performance and Mechanism of MgO Meso-/Macroporous Nanostructures for Simultaneous Removal of As(III) and F in a Groundwater System. *Environ. Sci.: Nano* **2016**, *3* (6), 1416−1424.
(37) Sharma, L.; Kakkar, R. Hierarchical Porous Magnesium Oxide (Hr-MgO) Microspheres for Adsorption of an Organophosphate Pesticide: Kinetics, Isotherm, Thermodynamics, and DFT Studies. *ACS Appl. Mater. Interfaces* **2017**, *9* (44), 38629−38642.
(38) Casey, P.; Hughes, G.; O'Connor, E.; Long, R. D.; Hurley, P. K. Growth and Characterisation of Thin MgO Layers on Si(100) Surfaces. *J. Phys.: Conf. Ser.* **2008**, *100* (4), 042046.
(39) López, I.; Utrilla, A. D.; Nogales, E.; Méndez, B.; Piqueras, J.; Peche, A.; Ramírez-Castellanos, J.; González-Calbet, J. M. In-Doped Gallium Oxide Micro- and Nanostructures: Morphology, Structure, and Luminescence Properties. *J. Phys. Chem. C* **2012**, *116* (6), 3935−3943.
(40) Mahmoodinezhad, A.; Janowitz, C.; Naumann, F.; Plate, P.; Gargouri, H.; Henkel, K.; Schmeißer, D.; Flege, J. I. Low-Temperature Growth of Gallium Oxide Thin Films by Plasma-Enhanced Atomic Layer Deposition. *J. Vac. Sci. Technol., A* **2020**, *38* (2), 022404.
(41) Onuma, T.; Fujioka, S.; Yamaguchi, T.; Itoh, Y.; Higashiwaki, M.; Sasaki, K.; Masui, T.; Honda, T. Polarized Raman Spectra in β-Ga_2O_3 Single Crystals. *J. Cryst. Growth* **2014**, *401*, 330−333.
(42) Wu, D.; Bai, Y.; Wang, W.; Xia, H.; Tan, F.; Zhang, S.; Su, B.; Wang, X.; Qiao, X.; Wong, P. K. Highly Pure MgO_2 Nanoparticles as Robust Solid Oxidant for Enhanced Fenton-like Degradation of Organic Contaminants. *J. Hazard. Mater.* **2019**, *374*, 319−328.
(43) Rafique, S.; Han, L.; Zhao, H. (Invited) Ultrawide Bandgap β-Ga_2O_3 Thin Films: Growths, Properties and Devices. *ECS Trans.* **2017**, *80* (7), 203−216.
(44) Feng, B.; Li, Z.; Cheng, F.; Xu, L.; Liu, T.; Huang, Z.; Li, F.; Feng, J.; Chen, X.; Wu, Y.; He, G.; Ding, S. Investigation of β-Ga_2O_3 Film Growth Mechanism on c-Plane Sapphire Substrate by Ozone Molecular Beam Epitaxy. *Phys. Status Solidi A* **2021**, *218* (4), 2000457.
(45) Wei, J.; Kim, K.; Liu, F.; Wang, P.; Zheng, X.; Chen, Z.; Wang, D.; Imran, A.; Rong, X.; Yang, X.; Xu, F.; Yang, J.; Shen, B.; Wang, X. β-Ga_2O_3 Thin Film Grown on Sapphire Substrate by Plasma-Assisted Molecular Beam Epitaxy. *J. Semicond.* **2019**, *40* (1), 012802.
(46) Seiler, W.; Selmane, M.; Abdelouhadi, K.; Perrière, J. Epitaxial Growth of Gallium Oxide Films on C-Cut Sapphire Substrate. *Thin Solid Films* **2015**, *589*, 556−562.
(47) Toliopoulos, D.; Fedorov, A.; Bietti, S.; Bollani, M.; Bonera, E.; Ballabio, A.; Isella, G.; Bouabdellaoui, M.; Abbarchi, M.; Tsukamoto, S.; Sanguinetti, S. Solid-State Dewetting Dynamics of Amorphous Ge Thin Films on Silicon Dioxide Substrates. *Nanomaterials* **2020**, *10* (12), 2542.
(48) Liang, G.; Cheng, L.; Zha, J.; Cao, H.; Zhang, J.; Liu, Q.; Bao, M.; Liu, J.; Zhai, X. In-Situ Quantification of the Surface Roughness for Facile Fabrications of Atomically Smooth Thin Films. *Nano Res.* **2022**, *15* (2), 1654−1659.
(49) Chen, R.; Wang, D.; Liu, J.; Feng, B.; Zhu, H.; Han, X.; Luan, C.; Ma, J.; Xiao, H. Ta-Doped Ga_2O_3 Epitaxial Films on Porous p-GaN Substrates: Structure and Self-Powered Solar-Blind Photodetectors. *Cryst. Growth Des.* **2022**, *22* (9), 5285−5292.
(50) Chen, Z.; Ge, K.; Meng, D.; Chen, X. Pure-Phase Ga_2O_3 Films Were Deposited on Sapphire Substrates by Radio Frequency Magnetron Sputtering. *Mater. Lett.* **2022**, *320*, 132385.
(51) Galazka, Z. β-Ga_2O_3 for Wide-Bandgap Electronics and Optoelectronics. *Semicond. Sci. Technol.* **2018**, *33* (11), 113001.
(52) Onuma, T.; Fujioka, S.; Yamaguchi, T.; Higashiwaki, M.; Sasaki, K.; Masui, T.; Honda, T. Correlation between Blue Luminescence Intensity and Resistivity in β-Ga_2O_3 Single Crystals. *Appl. Phys. Lett.* **2013**, *103* (4), 041910.
(53) Nefedova, V. E.; Fröhlich, S.; Navarrete, F.; Tancogne-Dejean, N.; Franz, D.; Hamdou, A.; Kaassamani, S.; Gauthier, D.; Nicolas, R.; Jargot, G.; Hanna, M.; Georges, P.; Ciappina, M. F.; Thumm, U.; Boutu, W.; Merdji, H. Enhanced Extreme Ultraviolet High-Harmonic Generation from Chromium-Doped Magnesium Oxide. *Appl. Phys. Lett.* **2021**, *118* (20), 201103.
(54) Bhakta, S.; Sahoo, P. K. Tuning Optical Bandgap of Crystalline MgO by MeV Co Ion Beam Induced Defects. *Appl. Phys. A: Mater. Sci. Process.* **2022**, *128* (11), 990.
(55) Roessler, D. M.; Walker, W. C. Electronic Spectrum and Ultraviolet Optical Properties of Crystalline MgO. *Phys. Rev.* **1967**, *159* (3), 733−738.
(56) Bensaid, D.; Ameri, M.; Benseddik, N.; Mir, A.; Bouzouira, N. E.; Benzoudji, F. Band Gap Engineering of Cd_{1-x} Be_xSe Alloys″. *Int. J. Met.* **2014**, *2014*, 1−7.

https://doi.org/10.1021/acsaom.3c00237
ACS Appl. Opt. Mater. 2023, 1, 1670−1678